POLITECNICO DI TORINO
Repository ISTITUZIONALE

Estimating geometric tortuosity of saturated rocks from micro-CT images using percolation theory

Original
Estimating geometric tortuosity of saturated rocks from micro-CT images using percolation theory / Panini, F., Ghanbarian, B., Salina Borello, E., Viberti, D.. - In: TRANSPORT IN POROUS MEDIA. - ISSN 0169-3913. - ELETTRONICO. - 151:(2024), pp. 1579-1606. [10.1007/s11242-024-02085-w]

Availability:
This version is available at: 11583/2988348 since: 2024-05-30T14:06:31Z

Publisher:
Springer

Published
DOI:10.1007/s11242-024-02085-w

Terms of use:

This article is made available under terms and conditions as specified in the corresponding bibliographic description in the repository

Publisher copyright
Springer postprint/Author's Accepted Manuscript

This version of the article has been accepted for publication, after peer review (when applicable) and is subject to Springer Nature's AM terms of use, but is not the Version of Record and does not reflect post-acceptance improvements, or any corrections. The Version of Record is available online at: http://dx.doi.org/10.1007/s11242-024-02085-w

(Article begins on next page)

19 November 2026

Estimating geometric tortuosity of saturated rocks from micro-CT images using percolation theory

Filippo Panini[1], Behzad Ghanbarian[2*], Eloisa Salina Borello[1], Dario Viberti[1]

[1] Department of Environment, Land and Infrastructure Engineering, Politecnico di Torino, Torino, Italy

[2] Porous Media Research Lab, Department of Geology, Kansas State University, Manhattan KS, USA

[*] Corresponding author's email address: ghanbarian@ksu.edu

Abstract. Tortuosity (τ) is one of the key parameters controlling flow and transport in porous media. Although the concept of tortuosity is straightforward, its estimation in porous media has yet been challenging. Most models proposed in the literature are either empirical or semi-empirical including some parameters whose values and their estimations are in prior unknown. In this study, we modified a previously presented geometric tortuosity (τ_g) model based on percolation theory and validated it against a methodology based on the pathfinding A* algorithm. For this purpose, we selected 12 different porous materials including four sandstones, three carbonates, one salt, and four synthetic media. For all samples, five sub-volumes at different lengths with fifty iterations were randomly selected except one carbonate sample for which three sub-volumes were extracted. Pore space properties, such as pore radius, throat radius, throat length, and coordination number distributions were determined by extracting the pore network of each sub-volume. The average and maximum coordination numbers and minimum throat length were used to estimate the τ_g. Comparison with the A* algorithm results showed that the modified model estimated the τ_g accurately with absolute relative errors less than 28%. We also estimated the τ_g using two other models presented in the literature as well as the original percolation-based tortuosity model. We found that our proposed model showed a significantly higher accuracy. Results also indicated more precise estimations at the larger length scales demonstrating the effect of uncertainties at the smaller scales.

Keywords: Finite size scaling, Percolation theory, Geometric tortuosity, Micro CT, Pathfinding, Pore network

1 Introduction

Understanding factors controlling flow and transport in porous media is essential and has broad applications to reservoir and geotechnical engineering, hydrogeology, and subsurface hydrology. One of these factors is tortuosity whose estimation at small and large scales has been under investigation. Four main types of tortuosity defined in

the technical literature are: (1) hydraulic, (2) geometric, (3) electrical, and (4) diffusive (Clennell, 1997). Hydraulic tortuosity is the square of the ratio of flux-weighted average path length to straight-line length and involves numerical simulation of fluid flow through a sample (Zhang et al., 2020). Electrical and diffusive tortuosity take into account the average flow paths for electrical flow and the average length of a chemical's diffusive pathway, respectively (Ghanbarian et al., 2013a). In this study, we, however, focus on geometric tortuosity, which is defined as the ratio of the average length of geometric flow paths (or shortest pathways) through the medium, $\langle L_g \rangle$, to the straight-line length, L_s, and is mathematically expressed ass (Ghanbarian et al., 2013a)

$$\tau_g = \frac{\langle L_g \rangle}{L_s} \quad (1)$$

Detailed descriptions of various types of tortuosity and their calculations in 2- and 3-D porous media can be found in Ghanbarian et al. (2013a) and Fu et al. (2021).

There exist different methods to determine the value of τ_g in porous media including theoretical models (Yu and Li, 2004; Ghanbarian et al., 2013b), empirical relationships (Jarrar et al., 2021), and numerical approaches (Sobieski, 2022). For instance, by assuming that a porous medium was composed of two-dimensional square solid particles, Yu and Li (2004) derived the following geometric tortuosity model:

$$\tau_g = \frac{1}{2}\left[1 + \frac{1}{2}\sqrt{1-\phi} + \frac{\sqrt{\left(1-\sqrt{1-\phi}\right)^2 + (1-\phi)/4}}{1-\sqrt{1-\phi}}\right] \quad (2)$$

where ϕ is the porosity. Although developed for two-dimensional media, the porosity-dependent model of Yu and Li (2004) was widely applied in the literature to estimate tortuosity from porosity (Wu et al., 2008; Tang and Lu, 2014; Huang et al., 2018; Liu et al., 2020; Wen et al., 2021) due to its simplicity, requiring only porosity as an input.

More recently, Avila et al. (2022) numerically calculated geometric tortuosity in three-dimensional porous media using the A* algorithm (Hart et al., 1968) and proposed an empirical model to estimate τ_g from porosity as follows

$$\tau_g = 5.98e^{-7.666\phi} + 1.44e^{-0.3665\phi} \quad (3)$$

Their model, however, was developed based on media whose porosities ranged between 0.5 and 0.9.

With recent advances in imaging techniques and high-performance computing, approaches based on image processing and pathfinding algorithms have been developed to determine the τ_g. For instance, pathfinding (or shortest path) algorithms have been successfully applied for the geometrical analysis of pore space and characterization of the microstructure of 2- and 3-D rock images. Such algorithms were also employed to characterize porous materials with industrial applications, such as metallographic powdered materials (Montes et al., 2007) and fuel cells (Cecen et al., 2012). The two most popular pathfinding algorithms are Dijkstra's (Dijkstra, 1959) and A* (Hart et al., 1968). The latter is an extension of the Dijkstra algorithm. Sun et al. (2011) used a shortest-path approach based on Dijkstra's algorithm to calculate the τ_g and connected

porosity to speed up and improve the accuracy of upscaled permeability estimations. Later, in a series of papers, Viberti et al. (2020), Panini et al. (2022) and Salina Borello et al. (2022) used the A* algorithm to describe the pore structure of 2- and 3-D binary images of rocks. They calculated τ_g, effective porosity, pore size distribution, and constriction factor based on the shortest paths information. The A* algorithm was also applied for the design and characterization of micromodels (Massimiani et al., 2023a; 2023b) and for the quantitative characterization of marble natural aging (Peter et al., 2023).

In another study, Amien et al. (2019) used a simple neurite tracer method to track connected pores and calculate the τ_g. They applied this method to two different cases: directly to images of porous media and to skeleton images extracted from original ones. They showed that values of τ_g were comparable between the two cases in simple porous media, but they differed in more complex systems. This means that the skeletonization might not produce an accurate representation of the pore space when the level of complexity and heterogeneity increases in porous media.

Jarrar et al. (2021) studied the τ_g in variably-saturated and unconsolidated sand packs. They calculated the value of τ_g from 3-D computed tomography images using a module available in PerGeos software. Jarrar et al. (2021) then proposed an empirical relationship to explain the τ_g as a function of porosity, wetting-phase saturation, coefficient of curvature, and roundness of grains. Although their model was saturation-dependent, one can still estimate the τ_g at full saturation by setting wetting-phase saturation equal to one.

Although simple models have been proposed to estimate the τ_g mainly from porosity, there exist other factors, such as pore space characteristics (e.g., connectivity) and sample dimensions that may play critical roles. The main objectives of this study, therefore, are to: (1) propose a model to estimate the τ_g from 3-D CT images, (2) evaluate the proposed model with numerical values, and (3) compare its performance with that of three other models i.e., Eqs. (2), (3) and (4) proposed in the literature.

The rest of the article is organized as follows. In Section 2, we revisit and improve the theoretical model of Ghanbarian et al. (2013b), developed based on percolation theory and finite size scaling, to estimate τ_g from pore network properties. In Section 3, rock samples, pore network extraction and A* algorithm are described. Criteria for model evaluation are presented in Section 4. The τ_g values estimated via Eqs. (2)-(5) are compared with those determined numerically via the pathfinding algorithm A* for a variety of rock types and porous media in Section 5. We also address the effect of sample length on the τ_g. For the sake of comparison, hydraulic tortuosity values computed from numerical simulations of velocity in the largest domain size are reported in Appendix A.

2 The percolation theoretic model

Percolation theory provides a theoretical approach to study interconnectivity and its effects on flow and transport in porous media (Hunt et al., 2014; Sahimi, 2023). Using concepts of percolation theory and finite size scaling, Ghanbarian et al. (2013b) proposed the following theoretical model for the τ_g under fully-saturated conditions

$$\tau_g = \left[\frac{p - p_c + \left(\frac{C}{L_s}\right)^{\frac{1}{\nu}}}{1 - p_c}\right]^{\nu - \nu D_{opt}} , \quad (4)$$

where p is the occupation probability ($0 \leq p \leq 1$), p_c is the critical occupation probability, ν = 0.88 is the correlation length scaling exponent in three dimensions, D_{opt} =1.43 is the optimal path fractal dimension in three dimensions, and L_s is the linear size of a system. We should point out that Sheppard et al. (1999) found the shortest path fractal dimension equal to 1.43, very close to the backbone fractal dimension of 1.42, for the optimal path model in three dimensions (see their Table 3). The value of 1.43 is also close to the shortest path fractal dimension $D_{min} = 1.374$ for the random percolation model in three dimensions (Sheppard et al., 1999).

To apply Eq. (4) to estimate t_g in porous media, following Balberg (1987), Ghanbarian et al. (2013b) replaced p and p_c with porosity, ϕ, and critical porosity, ϕ_c. By comparing with experiments and simulations, Ghanbarian et al. (2013b) found reasonable τ_g estimations (see their Figures 3, 4 and 6). Eq. (4) with $C/L_s = 0$ also successfully estimated tortuosity in anisotropic carbon paper gas diffusion layers (Ghanbarian and Cheng, 2016).

In Eq. (4), *C* is the fundamental length scale whose value based on two-dimensional Monte Carlo simulations of percolation was found to be equal to 0.85 in units of the bond length (Kapitulnik et al., 1983). This means for the unit length of bond; the value of *C* would be 0.85. Although found based on two-dimensional simulations, Ghanbarian et al. (2013b) showed *C* = 0.85 in units of the bond length resulted in good agreement between theory and simulations in three dimensions (see their Figure 4b). Recently, Ghanbarian et al. (2023) demonstrated that in soils *C* can be approximated as $0.85 l_{tmin}$ in which l_{tmin} is the minimum throat length. Nonetheless, further investigations are still required to accurately determine the value of *C* in irregular networks of pores.

For two-dimensional regular lattices including square, hexagonal and triangular as well as three-dimensional ones including simple cubic, body-centered cubic, and face-centered cubic, Bernabé et al. (2010) showed that the occupation probability p varied linearly with the average pore coordination number Z_{ave} (see their Figure 1). Ghanbarian et al. (2021) used the same approach, modified the traditional finite-size scaling, and showed that the *Z*-based finite-size scaling analysis led to perfect collapse in scale-dependent permeability simulations in pore networks. Following Bernabe et al. (2010) and Ghanbarian et al. (2021), we replace p and p_c with respectively $\frac{Z_{ave}}{Z_{max}}$ and $\frac{1.5}{Z_{max}}$ and set *C* equal to $0.85 l_{tmin}$ in Eq. (4) to have

$$\tau_g = \left[\frac{\frac{Z_{avg}}{Z_{max}} - \frac{1.5}{Z_{max}} + \left(\frac{0.85 l_{tmin}}{L_s}\right)^{\frac{1}{\nu}}}{1 - \frac{1.5}{Z_{max}}} \right]^{\nu - \nu D_{opt}}, \quad (5)$$

where Z_{avg} is the volume-weighted average coordination number and Z_{max} is the maximum pore coordination number. The coordination number is the number of throats connected to a pore and Z_{avg}, Z_{max} and l_{tmin} are obtained by pore network extraction, as we explain in Section 3.2. In Eq. (5), $Z_c \approx 1.5$ in three dimensions is the percolation threshold expressed in terms of the coordination number (Bernabe et al., 2010), and $\frac{1.5}{Z_{max}}$ represents its normalized value.

Eq. (5), presented here for the first time, has not yet been evaluated in the estimation of the τ_g for different types of porous media. Nor has it been compared with A* algorithm estimations.

3 Materials and Methods

3.1 Rock samples

To study geometric tortuosity and its estimation, we selected 12 different samples from a wide range of porous media including four synthetic and eight natural rocks with different porosity values. The natural rock samples consisted of four sandstones, three carbonates, and one salt, while the synthetic media included two synthetic samples generated by the QSGS algorithm (Wang et al., 2007), one synthetic texturally equilibrated porous medium, and one synthetic sphere pack. The rock computed tomography (CT) images were collected from the Digital Rock Portal[1] and the Imperial College London websites[2]. The four sandstones included Berea, Bentheimer (Imperial College Consortium on Pore-scale Imaging and Modelling, 2014a and 2015a), Parker and Leopard (Neumann et al., 2020). The three carbonates included Ketton, Carbonate C1, and Carbonate C2 (Imperial College Consortium on Pore-scale Imaging and Modelling, 2015b, 2014b and 2014c). The salt sample was obtained from Ghanbarzadeh (2015), the synthetic texturally-equilibrated porous medium from Ghanbarzadeh et al. (2016), and the synthetic sphere pack from Finney (2016). The two samples generated by the QSGS algorithm were from Salina Borello et al. (2022). Fig. 1 shows the images of the samples used in this study.

For each rock sample, 250 subsamples characterized by five different length scales (

Fig. 2) were randomly extracted to investigate the effect of length scale on the tortuosity estimation. In particular, for each length scale 50 subsamples (subdomains) were selected. For carbonate C2, all the subsamples with length scales smaller than 41^3 voxels were not considered because of the absence of connectivity.

[1] https://www.digitalrocksportal.org/projects/

[2] https://www.imperial.ac.uk/earth-science/research/research-groups/pore-scale-modelling/micro-ct-images-and-networks/

In total, 3012 samples were analyzed, representative of several different lithologies and a wide range of porosity (from 7% to 37%). Properties of the samples, such as image resolution, dimension, and porosity, and their corresponding network characteristics are summarized in

Table **A1** in Appendix A.

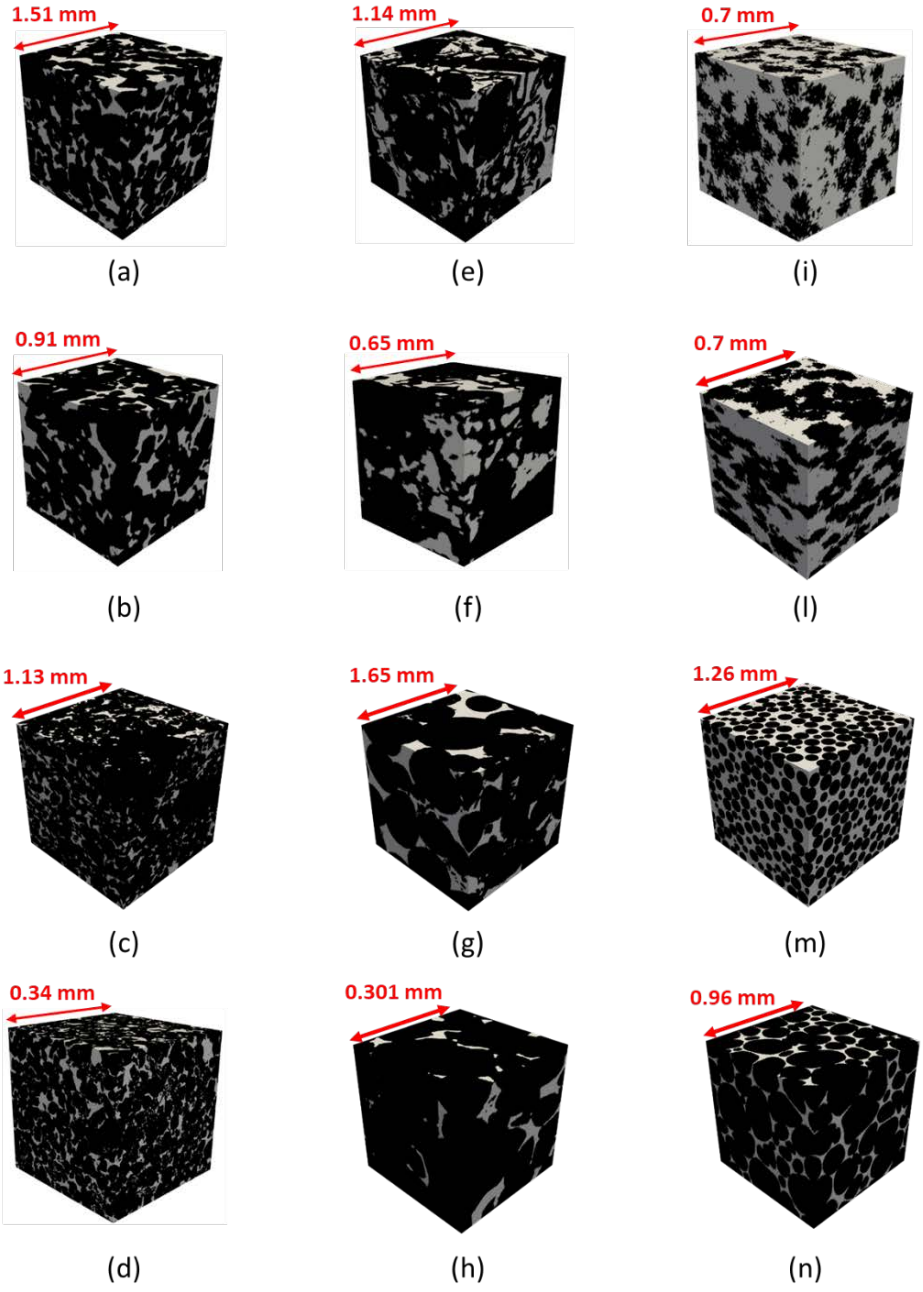


Fig. 1 Initial images of sandstones Bentheimer (a), Berea (b), Parker (c) and Leopard (d); carbonates C1(e), C2 (f), and Ketton (g); salt (h); synthetic media QSGS isotropic (i), QSGS anisotropic (l), Finney (m), and RG_theta60 (n). Grains are represented in white, while pores in black.

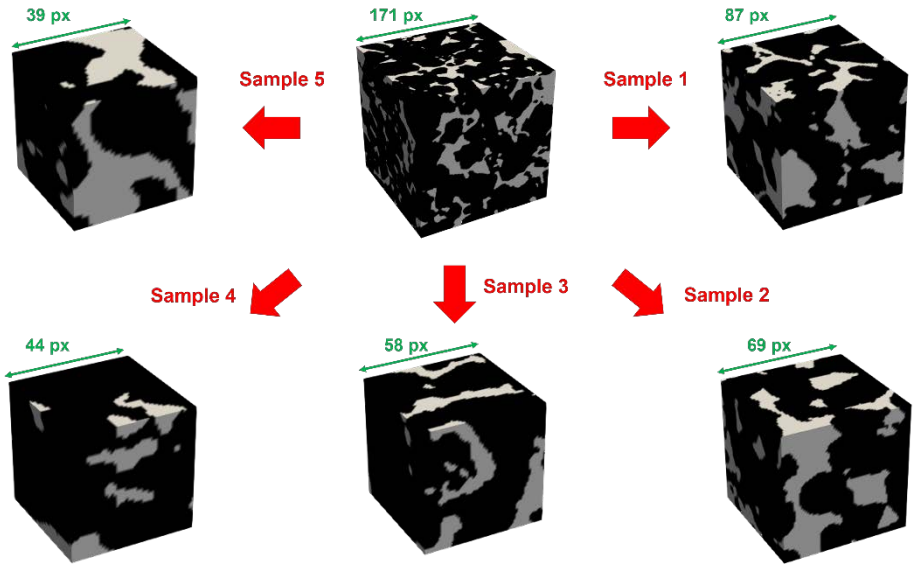


Fig. 2 Five sub-volumes with different length scales extracted from the original image for the Berea sandstone sample.

3.2 Pore network extraction and its characterization

To estimate the τ_g via the proposed theoretic model, Eq. (5), one needs to extract the pore network of a porous medium from its micro-CT image and determine pore-network characteristics, such as the average and maximum pore coordination numbers and the minimum throat length (Z_{ave}, Z_{max} and l_{tmin}). A pore network is a representation of the 3D image, where the network elements follow the pore space geometry (Raeini et al., 2017). Pore-network modeling, i.e., generating a pore network that represents the pore space and simulating flow in such a network, is a common approach to estimate petrophysical and pore-scale properties of a rock from its micro-CT image. The idea behind this method is to construct a simplified geometrical representation of the pore space, preserving all the geometrical information needed to understand the fluid flow (Blunt, 2017). Within this simplification approach, the pore space is represented by pores, usually spheres (wider regions), connected by throats (narrower regions). To distinguish between pore and throat in a CT image, the maximal ball algorithm and image

analysis techniques were proposed (Raeini et al., 2017; Yi et al., 2017). In the pore networks extracted here, pores were assumed to be spherical and throats cylindrical. An important geometrical parameter of pore networks quantifying pore connectivity is the coordination number (Z), which is the number of throats connected to a single pore (An et al., 2016).

Pore network extraction from 3D micro-CT images is a crucial step for the calculation of τ_g using Eq. (5) and therefore the choice of the algorithm affects the results. In this study, we used the open-access code *pnextract*, developed Raeini et al. (2017) at the Imperial College London[3], which was widely applied in the literature (Raeini et al., 2019; Garfi et al., 2020; Foroughi et al., 2021; Niu et al., 2022). In order to identify pores and throats, the first step of the algorithm is to calculate the distance between each voxel and the nearest solid wall to create a distance map. Then, the medial surface of the pore space is extracted with the purpose of improving the efficiency of the network extraction. Finally, using the medial surface, pores and throats are identified using maximal-sphere hierarchy. A detailed description of the methods implemented in *pnextract* was given by Raeini et al. (2017), in particular see Stages 1 and 2 of the algorithm.

Parameters extracted from the micro-CT images were coordination number, pore radius, throat radius, and throat length distributions (**Fig. 3**). Values of maximum coordination number and minimum throat length were calculated from the histograms of the extracted parameters for each micro-CT image sample and sub-volume. Then, they were used to estimate the τ_g via Eq. (5). The average value of the coordination number (Z_{avg}) used in Eq. (5) was calculated as a weighted average based on the pore volumes as follows

$$Z_{avg} = \frac{\sum_{i=1}^{n} Z_i V_i}{\sum_{i=1}^{n} V_i}, \tag{6}$$

where V_i is the volume of the pore with coordination number Z_i. In this way, pores with larger volumes contribute more to the average because physically they contribute more to the fluid displacement.

The values of the weighted average coordination number ($\bar{Z}_{ave}$), minimum coordination number ($\bar{Z}_{min}$) and minimum throat length ($\bar{l}_{tmin}$) averaged over fifty subsamples for each length scale are reported in Table A1 in Appendix A.

[3] https://github.com/ImperialCollegeLondon/pnextract

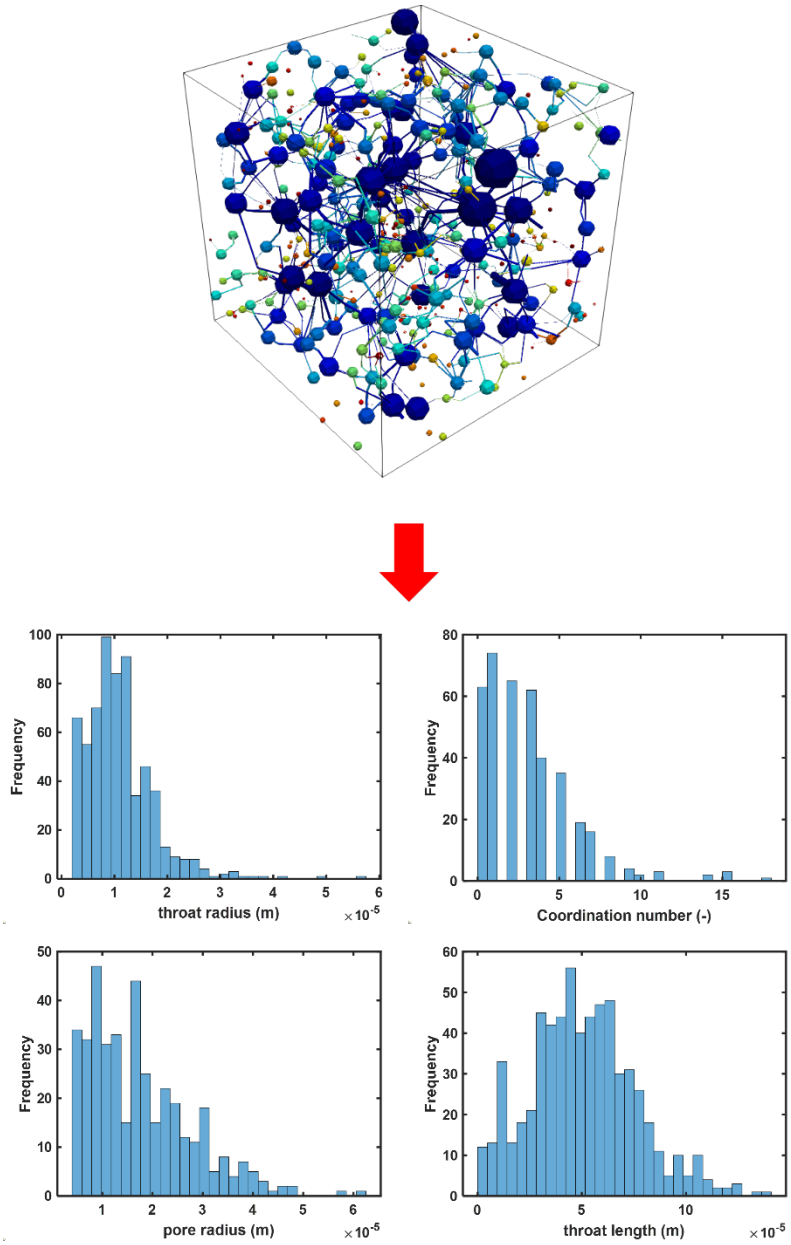


Fig. 3 Example of the extracted pore network for the Berea sandstone and corresponding throat radius, coordination number, pore radius, and throat length histograms.

3.3 A* algorithm

In this study, the A* algorithm was used to compute the shortest paths between each inlet-outlet pair (Hart et al., 1968; Nilsson, 1980; Nilsson, 2014).

According to the literature, A* is the most popular technique for identifying minimum paths in the presence of obstacles (Candra et al., 2020) because of its optimality (i.e. the output is the best solution according to the criteria), efficiency (other path finding algorithms, e.g. Dijkstra, will take more time, computational resources or both) (Candra et al., 2020; Foead et al., 2021; Martell and Sandberg, 2016; Permana et al., 2018; Rachmawati and Gustin, 2020), and completeness (if at least one solution exists then the algorithm is guaranteed to find a solution in a finite amount of time) (Russell and Norvig, 2021). Validation of the methodology applied to pore structure characterization were presented in the literature (Viberti et al., 2020; Panini et al., 2022; Salina Borello et al., 2022; Ávila et al., 2022).

The process is achieved by the following steps. Starting from an inlet location ($n = n_0$), at each step the algorithm expands the current node n by exploring all nodes n_i, called successors, in the proximity of n. Then, for the successors n_i, the following cost function is evaluated:

$$c(n_i) = g(n_i) + h(n_i), \tag{7}$$

where i indicates the i^{th} successor of n, $g(n_i)$ is the backward cost i.e., the distance calculated over the incremental path already identified from the inlet to n_i, and $h(n_i)$ is the forward cost i.e., a heuristic function representing the estimation of the cost to move from n_i to the target (outlet). The Euclidean distance was adopted as forward cost $h(n_i)$. Then, the algorithm moves from node n to the node having the lowest cost among all explored and unexpanded nodes (i.e., nodes where the cost function has already been calculated and successors have not been explored yet). The calculation is repeated until the target point is reached. Then, the path is constructed backward from the target point to the inlet point by connecting the parent nodes. Further details about the A* algorithm with applications to rock characterization can be found in Viberti et al. (2020), Panini et al. (2022), and Salina Borello et al. (2022).

For 3-D images, an algorithm based on medial axis and cluster analysis was developed in order to place inlet and outlet points uniformly distributed over the surface automatically (Salina Borello et al., 2022). The geometric tortuosity $\tau_{g,i}$ in the i direction can be calculated by (Salina Borello et al., 2022):

$$\tau_{g,i} = \frac{\langle L_{sh,i} \rangle}{L_i} \quad \text{where } i = x, y, z \tag{8}$$

in which $\langle L_{sh,i} \rangle$ is calculated as the average of the shortest path lengths calculated using the A* algorithm and L_i is the length of the sample in i direction.

Then, the geometric mean of the three directional values of tortuosity was calculated in analogy with the isotropic equivalent permeability (Muskat, 1938):

$$\tau_g = \sqrt[3]{\tau_{g,x}\, \tau_{g,y}\, \tau_{g,z}} \tag{9}$$

In order to measure the minimum number of inlets/outlets required for a reliable characterization of the geometric properties of the sample, a preliminary sensitivity analysis of geometric tortuosity with respect to the number of considered inlet (n_{in}) and outlet points (n_{out}) was conducted. We selected the Berea sandstone (Berea_ini in Table A1) for the sensitivity analysis because it had sufficient complexity and porosity to be considered representative of all the other rocks. Simulations were conducted using $n_{in} = n_{out} = 50$, 30, and 20. The sensitivity to the average tortuosity value was trivial, with variations less than 1 %. More specifically, we found τ_g = 1.415, 1.411, and 1.412 using 50, 30, and 20 points, respectively. Moreover, the calculated geometric tortuosity was comparable with the value obtained for a 2D section of Berea presented reported by Viberti et al. (2020). Thus, we decided to use $n_{in} = n_{out} = 20$ for the sake of reducing the computational effort.

4 Models evaluation criteria

To evaluate the accuracy of Eqs. (2)-(5) in the estimation of τ_g, the absolute relative error, ARE, and the corrected Akaike Information Criterion, AIC_c, (Akaike, 1974; Hurvich et al., 1989) were calculated as follows:

$$ARE = \frac{|\tau_{g,est} - \tau_{g,A*}|}{\tau_{g,A*}} \times 100, \tag{10}$$

$$AIC_c = 2q + N \ln\left(\frac{\mathrm{RSS}}{N}\right) + \frac{2q(q+1)}{N-q-1}, \tag{11}$$

where $\tau_{g,est}$ is the estimated τ_g via Eqs. (2)-(5), $\tau_{g,A*}$ is the geometric tortuosity calculated via the A* algorithm and Eq. (9), N is the number of samples, q is the number of model input parameters, and RSS is the residual sum of squares. The AIC_c allows comparing the performance of models of different numbers of input parameters. The smaller the AIC_c, the more accurate the model.

5 Results and discussion

In this section, we present the τ_g values estimated using the proposed percolation-based model, Eq. (5), and compare them with those determined via the A* pathfinding approach, Eq. (9). Comparisons with the percolation-based model of Ghanbarian et al. (2013b), Eq. (4) with p and p_c respectively replaced by ϕ and ϕ_c (=0.1ϕ), the analytical models of Yu and Li (2004), Eq. (2), and the empirical model of Avila et al. (2022), Eq. (3), are also provided. To estimate the τ_g via Eq. (4), we set $C = 0.85 l_{tmin}$. For the sake of comparison, we also computed the hydraulic tortuosity, τ_h, using the numerical simulations via OpenFoam for the largest rock domain size (see Appendix A for details). As also argued by Ghanbarian et al., (2013a), we demonstrate that one should expect $\tau_h \approx \tau_g$ in relatively homogenous media. We present the obtained results in Fig. 4-9 and summarize them in Tables A2 and A3 in Appendix A.

Fig. 4 compares τ_g values estimated via Eq. (5) with those computed using the A* algorithm. To investigate uncertainties in the estimation, we plotted the τ_g against the sub-volumes of five different linear sizes for all samples. Comparison with the full sample (dashed line) is also reported. Values of each group of subsamples, corresponding to the same rock and with the same length scale, are shown in the form of a boxplot. Each box height represents the interquartile range (IQR) of the distribution over the subsamples, i.e., the distance between the 25th and the 75th percentile; the line inside the box represents the median; the vertical segments, called "whiskers", are delimited by the minimum and maximum values not considered as outliers; the latter are plotted individually as crosses.

Generally speaking, larger variations within the subsamples were observed for the τ_g values estimated by Eq. (5) and for more complex porous media, such as carbonate C1, anisotropic QSGS, and Salt. In general, the τ_g values are more spread when estimated with Eq. (5) than computed with the A* algorithm. In more homogeneous media, such as Finney and RG, the IQR does not change greatly across the length scales. For the other samples, however, an increasing trend in the IQR was observed by decreasing the sample size, and most of the samples exhibited the smallest IQR at the largest sample size (L_1). Generally speaking, one should expect higher variability and uncertainties for smaller heterogeneous media, especially for rocks with more complex structures. Thus, the larger the sample size, the more accurate the τ_g estimation is expected. Uncertainties at smaller scales may be improved by increasing the number of subsamples (or realizations). One should note that one of the limitations of the A* algorithm is that it works only if interconnected paths exist between inlet and outlet points, and they must exist in all three directions in order to apply Eq. (9). In low-porosity or strongly anisotropic porous media, such as C2 and Salt, only a few interconnected paths were present.

Fig. 5 compares the τ_g, averaged over 50 subsamples, estimated via Eqs. (2)-(5) against that computed using the A* algorithm. The 1:1 line is represented via a solid line, and the factor of 1.5 confidence intervals by dashed lines. For some subsamples, particularly in low-porosity rock samples, such as C1_carb, C2_carb, Parker, Leopard and Salt, there existed no interconnected paths between the inlet and outlet points and, therefore, no τ_g value was determined. That is why the number of subsamples used to calculate the τ_g for some sub-volumes, reported in Table A2, is less than fifty. We should point out that we did not report scenarios with less than 10 subsamples, such as C2_carb_n2, Salt_n4, and Salt_n5 listed in Table A2. It was verified that in these scenarios, generating new random subsamples could not produce a significant number of additional interconnected paths.

To estimate the τ_g via Eqs. (4) and (5), one needs to determine the value of C. As stated earlier, following Ghanbarian et al. (2023), we set $C = 0.85 l_{tmin}$. In addition to the minimum l_t value, we estimated C from median and mean values of l_t, determined from the throat length distribution, and found less accurate estimations (results not shown). This means $C = 0.85 l_{tmin}$ is a reasonable approximation.

Fig. 5 clearly demonstrates that Eqs. (2) and (3), represented by red and blue unfilled circles respectively, substantially overestimated the τ_g in complex porous media, such

as natural rocks. In fact, we found only a few estimations within the factor of 1.5 confidence intervals. Although Eq. (4) outperformed Eqs. (2) and (3), it overestimated the τ_g. More specifically, we found that a few estimations by Eq. (4) were out of the confidence intervals. The τ_g estimations via Eq. (5), however, were distributed around the 1:1 line within the factor of 1.5 confidence intervals.

Fig. 6 shows the ARE values for the τ_g estimations via Eqs. (2)-(5) as well as their averages over all samples. For the sample number, see Table A2. The ARE averaged over all rock samples was 124% for the Yu and Li (2004) model, Eq. (2), 92% for the Avila et al. (2022) model, Eq. (3), 32% for the Ghanbarian et al. (2013b) model, Eq. (4), and 12% for the revisited percolation-based model, Eq. (5).

Fig. 7 shows boxplots of the distribution of AIC_c calculated by comparing the estimated τ_g via Eqs. (2)-(5) with those computed using the A* algorithm. The AIC_c median value is 281 for Eq. (2), 255 for Eq. (3), 167 for Eq. (4), and 97 for Eq. (5). The red plus marks in Fig. 7 show two outliers. Both ARE and AIC_c analyses demonstrated that the percolation theory-based approaches (i.e., Eqs. (4) and (5)), accounting for minimum throat length and sample linear size, estimated the τ_g more accurately Eqs. (2) and (3). The τ_g model proposed by Yu and Li (2004) was developed for two-dimensional media based on oversimplifying assumptions. For instance, Yu and Li (2004) presumed a medium composed of equally spaced square-shaped particles with no contacts, meaning that the medium was well connected. The Avila et al. (2022) model is purely empirical, and because of its empiricism, the interpretation of its parameters and their variations from one porous medium to another is not clear. In addition to that, it is also well-documented in the literature that the accuracy and reliability of regression-based models are database-dependent (Ghanbarian and Pachepsky, 2022). This means that a regression-based model trained and tested using a database may fail to provide accurate estimates if evaluated further via an independent database (Schaap and Leij, 1998). The Avila et al. (2022) model was established using porous media with porosities in the range of 0.45 and 0.95. Accordingly, one should expect poor τ_g estimations via Eq. (3), if applied to porous media with porosities greatly less than 0.45.

The revisited percolation-based model presented, Eq. (5), incorporating the volume-weighted average coordination number and maximum pore coordination number, outperformed Eq. (4). Our results demonstrated that a better parametrization of the tortuosity model by incorporating pore space characteristics, such as connectivity proposed in this study can lead to substantially more accurate geometric tortuosity estimations in complex porous media, such as natural rocks. Moreover, the pore network extraction with *pnextract* does not require additional significant computational effort (seconds or few minutes on an office workstation).

We also investigated how the ARE value varied with the sample linear size (L_s) in the percolation approach (Fig. 8). To this end, sub-samples of all rock types were grouped into four L_s intervals i.e., 0-250 μm, 250-500 μm, 500-750 μm, and higher than 750 μm) and boxplots of ARE values were shown for each group. Fig. 8 exhibits a clear decreasing trend in the median ARE As can be seen, by increasing the length scale, the median ARE value decreased.

421 Finally, we studied the effect of voxel size on the τ_g estimation. Results are presented
422 in Fig. 9. For five different rock types (Bentheimer, Berea, Ketton, RG, and Salt), we
423 took one of the subsamples with the length scale L_1 and resampled the domain upscal-
424 ing the voxel dimension 2 and 3 times and downscaling up to 5 times. For each obtained
425 image, the porosity and pore network characteristics are reported in Table A3 in Ap-
426 pendix A, along with the estimated τ_g. Percolation-based geometric tortuosity, obtained
427 for the resampled 3-D images (Fig. 9), was sensitive to voxel size in most cases, both
428 in the case of figure upscaling and downscaling. However, the interquartile range main-
429 tained always below 20%.
430 For the sake of comparing geometric and hydraulic tortuosity values, we also com-
431 puted the hydraulic tortuosity, τ_h, by numerically simulating fluid flow and velocity at
432 the largest length scale i.e., L_1 (see Appendix A for detail). Results presented in Table
433 A2 show that the τ_h was greater than the τ_g in more heterogeneous media, while their
434 values are not greatly different in relatively homogeneous cases, in accord with the
435 Ghanbarian et al. (2013a) argument. We found the τ_h less than the τ_g by 2% for the
436 samples Leopard_ini and Finney_ini and by 6% for the sample C2_carb_ini. Such a
437 slight difference, however, is trivial. On average, we found the τ_h was 7% greater than
438 the τ_g. This means Eq. (5) can be used as an approximation in the estimation of τ_h when
439 velocity simulations are not available. However, further investigations are required to
440 address the accuracy and reliability of Eq. (5) in the estimation of τ_g and τ_h for a
441 broader range of porous media, such as soils and fracture networks, with various levels
442 of heterogeneity.

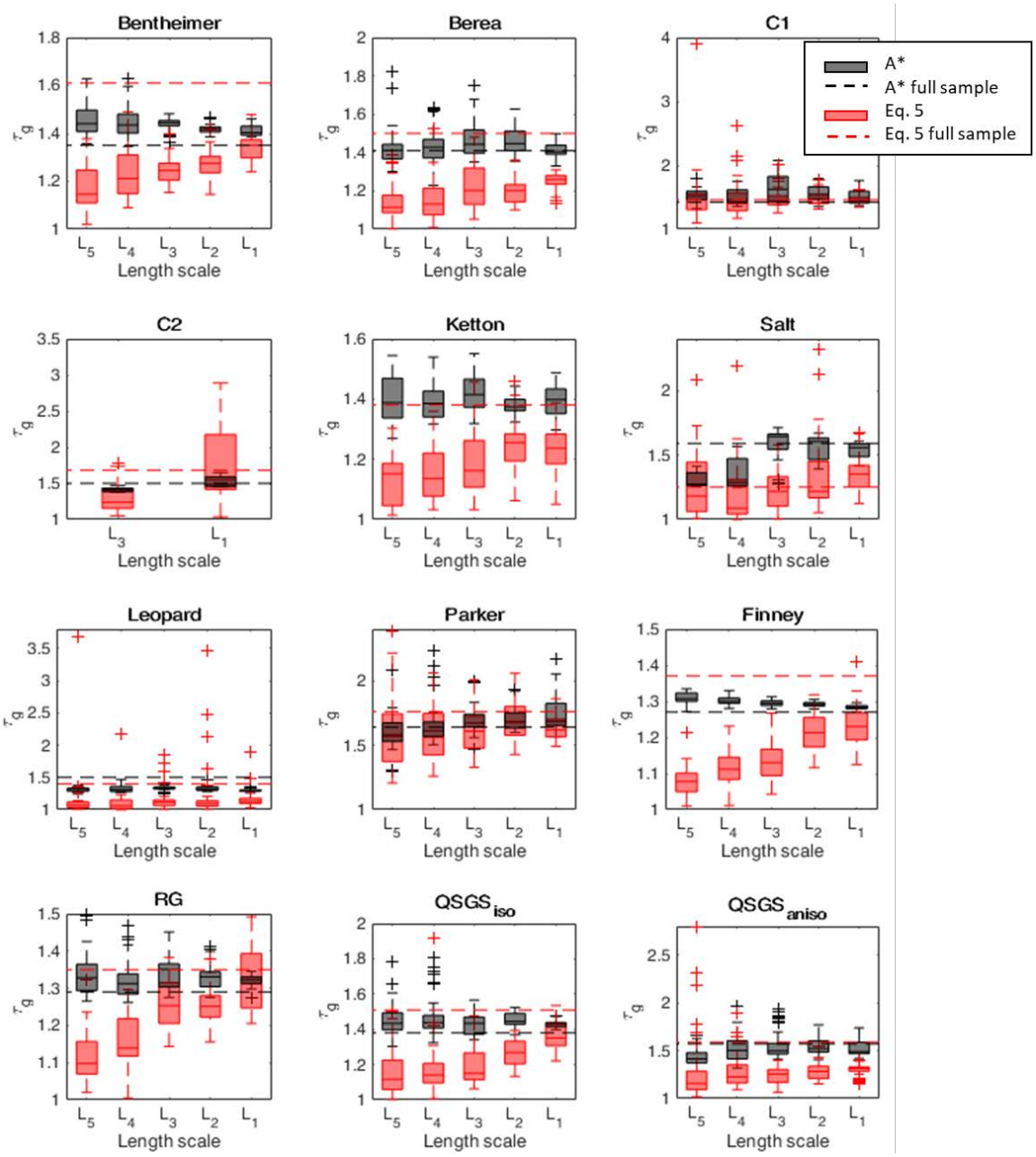


Fig. 4 Geometric tortuosity values of all the samples. On the horizontal axis, L_1 refers to the length of the largest sub-volumes and L_5 to the length of the smallest sub-volumes (see Table A2). Dashed lines represent the tortuosity estimated over the initial sample. Tortuosity values calculated with Eq. (5) are represented in red, while the tortuosity values calculated using the A* based methodology are represented in black.

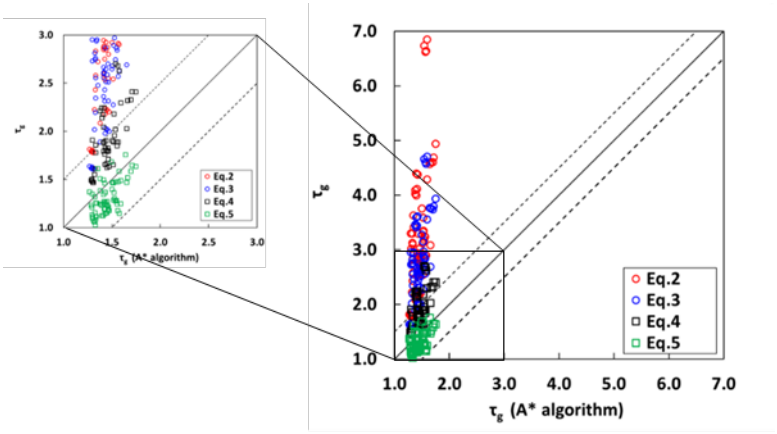


Fig. 5 τ_g estimated by the Yu and Li (2004) model, Eq. (2) shown by red unfilled circles, Avila et al. (2022) model, Eq. (3) shown by blue unfilled circles, Ghanbarian et al. (2013b) model, Eq. (4) shown by black unfilled squares, and the proposed percolation-based model, Eq. (5) shown by green unfilled squares, plotted against that computed via the A* algorithm. Dashed lines represent the factor of 1.5 confidence intervals, and the solid lines denote the 1:1 line.

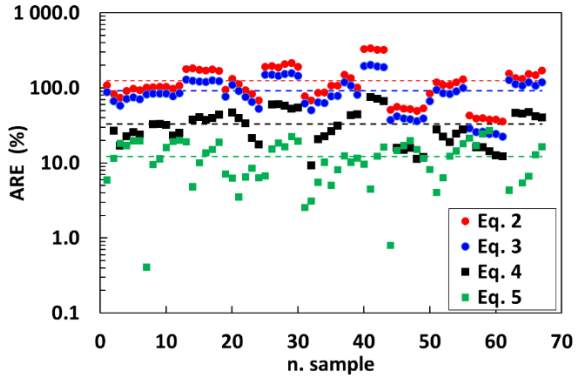


Fig. 6 Absolute relative error (***ARE***) for the τ_g (average value of the subsamples) estimated by the Yu and Li (2004) model, Eq. (2) (red filled circles), the Avila et al. (2022) model, Eq. (3) (blue filled circles), the Ghanbarian et al. (2013b) model, Eq. (4) shown by black filled squares, and the proposed percolation-based model, Eq. (5) shown by green filled squares. The average ***ARE*** values are reported as horizontal dashed lines. For sample number see Table A2 in Appendix A.

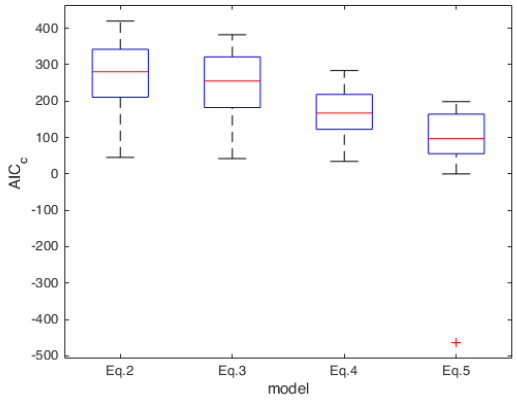


Fig. 7 Boxplots of the distribution of the Akaike information criterion ($\boldsymbol{AIC_c}$) for the $\boldsymbol{\tau_g}$ estimated by the Yu and Li (2004) model, Eq. (2), the Avila et al. (2022) model, Eq. (3), the Ghanbarian et al. (2013b) model, Eq. (4), and the proposed percolation-based model, Eq. (5). The red line represents the median $\boldsymbol{ARE}$ value. The red plus mark indicates an outlier.

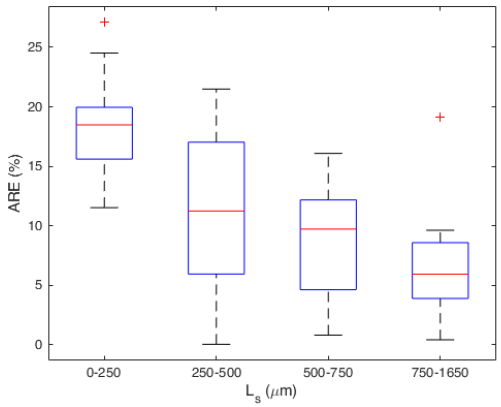


Fig. 8 Boxplot of the distribution of the absolute relative error ($\boldsymbol{ARE}$) for the $\boldsymbol{\tau_g}$ estimated by the proposed percolation-based model, Eq. (5), against the length of the sample ($\boldsymbol{L_s}$). The red line represents the median $\boldsymbol{ARE}$ value, and the red plus marks represent two outliers. As can be seen, by increasing the $\boldsymbol{L_s}$, the median $\boldsymbol{ARE}$ value decreased.

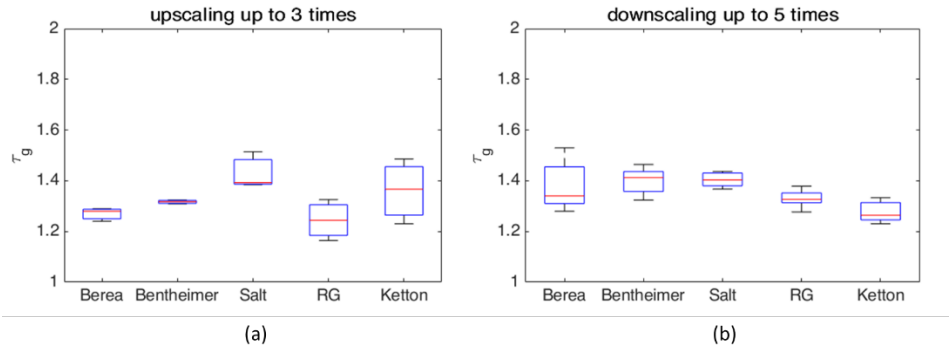


Fig. 9 Sensitivity analysis of the $\boldsymbol{\tau_g}$ to the voxel size by (a) upscaling and (b) downscaling of the same realization at the length scale $\boldsymbol{L_1}$.

6 Conclusions

In this study, we revisited the theoretic model proposed by Ghanbarian et al. (2013b) to estimate the geometric tortuosity, τ_g, from 3-D images of porous media. In the proposed model, the value of τ_g is estimated from the average pore coordination number, maximum pore coordination number, Z_{max}, minimum pore-throat length, l_{tmin}, and sample linear size, L_s. The proposed model was evaluated using the τ_g values computed via the A* algorithm for a variety of rock types and length scales. In all cases, the τ_g estimates were accurate, with an average absolute relative error (ARE) of 12%. We found more accurate estimations for samples with larger length scales. We also compared the performance of three other models including Yu and Li (2004), Eq. (2), Avila et al. (2022), Eq. (3), and Ghanbarian et al. (2013b), Eq. (4), in the estimation of τ_g. The calculated absolute relative error and Akaike information criterion showed that the model proposed in this study, Eq. (5), estimated the τ_g in saturated rocks at different scales much more accurately than the other three models. Particularly, Eqs. (2) and (3) substantially overestimated the value of τ_g. At the largest length scale, we also computed the hydraulic tortuosity, τ_h, by means of numerical simulations of fluid flow and velocity. Results showed that, on average, the τ_h was greater than the τ_g by 7%. This indicates that Eq. (5) can be applied as an approximation to estimate τ_h, when numerical simulation of velocity is not available. However, further investigations are still required to evaluate the reliability of Eq. (5) in the estimation of τ_g and τ_h for a broader range of porous media, such as soils and fracture networks, with various levels of heterogeneity.

Appendix A

Sample properties and their corresponding network characteristics are reported in

Table **A1**. For each rock, the full sample (subscript _ini) and the subsamples with decreasing length scale (subscripts _n1,… _n5) were characterized in terms of porosity ($\bar{\phi}$), average coordination number ($\bar{Z}_{ave}$), maximum coordination number ($\bar{Z}_{max}$) and minimum pore throat length ($\bar{l}_{tmin}$). For each subsample length scale, the reported values represent averages of over fifty different subsamples; the standard deviation is given in parentheses (see Table A1).

Results of the average geometric tortuosity estimated via Eqs. (2)-(5) for all subsamples and the relative error with respect to the A* algorithm are given in Table A2. The reported tortuosity values represent averages over several subsamples. Sample number, sample length (L_s), the number of subsamples used to calculate the average (No. of subsamples), and the geometric tortuosity simulated via the A* algorithm (Eq. 9) are also reported.

The hydraulic tortuosity along the i direction ($i = x, y, z$) was estimated from the simulated velocity values as (Koponen et al., 1996):

$$\tau_{h,i} = \frac{\langle |v| \rangle}{\langle v_i \rangle} \tag{A1}$$

where $|v| = \sqrt{v_x^2 + v_y^2 + v_z^2}$ is the magnitude of the local velocity, v_i is the directional component of the velocity, and $\langle\rangle$ indicates the average over the void space.

Single-phase fluid flow was simulated by the computational fluid dynamic modeling at low Reynolds numbers (i.e., Re < 1) to obtain steady state velocity field in the pore space. Simulations were performed using the software OpenFOAM 11 (Greenshields, 2023), based on the finite volume method (FVM). The FVM is an efficient technique for the computational modeling of single- and multi-phase flow problems in porous media and for the evaluation of hydraulic tortuosity and permeability (Ferrari and Lunati, 2013; Guibert et al., 2015; Soulaine et al., 2016; Rahmanian and Kantzas, 2018; Germanou et al., 2018). Using SnappyHexMesh, the native OpenFOAM mesh generator utility, a grid representing the pore space of the rock was generated starting from the raw binarized image files of the rock samples (see Section 3.1). The Navier-Stokes equations (NSEs) govern the incompressible single-phase flow at small Reynolds numbers. The NSEs were solved under the steady-state conditions using the SIMPLE algorithm (Patankar, 1980). The boundary conditions imposed were no-slip at the fluid-solid interface and constant pressure at the inlet and outlet. We verified that, under laminar flow, the estimated tortuosity was not sensitive to the imposed value of pressure gradient (Aminopour et al., 2018).

The τ_h values computed for the largest length scale using numerical simulations are reported Table A2. The sensitivity of the proposed percolation-based approach to the voxel dimension is presented in Table A3. For five different rock types (Berea, Bentheimer, Ketton, RG, and salt) the first realization of the subsample with length scale L_1 was considered. For each case the image was resized by upscaling up to a factor 3 and by downscaling up to a factor 5. The percolation-based τ_g model, Eq. (5), obtained for the resampled 3-D images are reported in Fig. 9. Sensitivity to voxel size is observable in most scenarios, both in the case of figure upscaling and downscaling. However, the interquartile range maintained always below 20%.

551 **Table A1** Sample properties and their corresponding network characteristics. Values
552 in parentheses represent one standard deviation.

Rock	Rock type	Voxel size (μm)	Sub-sample	Sample size (voxels)	$\bar{\phi}$ (-)	$\bar{Z}_{ave}$ (-)	$\bar{Z}_{max}$ (-)	$\bar{l}_{tmin}$ (μm)
Berea	Sandstone	5.345	Berea_ini	171^3	0.20	7.2	18.0	1.8
			Berea_n1	87^3	0.23 (0.012)	7.5 (0.94)	12.4 (2.09)	2.7 (0.98)
			Berea_n2	69^3	0.24 (0.034)	6.1 (1.45)	8.7 (1.82)	3.0 (1.55)
			Berea_n3	58^3	0.22 (0.053)	4.6 (0.94)	6.5 (0.93)	3.5 (1.86)
			Berea_n4	44^3	0.23 (0.075)	3.9 (1.01)	4.9 (1.39)	4.1 (1.97)
			Berea_n5	39^3	0.24 (0.080)	3.8 (0.93)	4.8 (1.14)	4.9 (2.89)
Bentheimer	Sandstone	9.404	Benth_ini	161^3	0.22	8.7	27.0	3.2
			Benth_n1	82^3	0.20 (0.007)	6.7 (0.28)	13.1 (1.61)	4.1 (1.62)
			Benth_n2	65^3	0.20 (0.011)	5.9 (0.38)	10.0 (1.41)	4.8 (1.76)
			Benth_n3	55^3	0.20 (0.017)	5.4 (0.44)	8.5 (1.11)	5.2 (2.12)
			Benth_n4	41^3	0.21 (0.034)	4.5 (0.70)	6.7 (1.07)	6.4 (2.69)
			Benth_n5	37^3	0.20 (0.042)	4.3 (0.61)	6.0 (1.12)	8.2 (4.20)
Parker	Sandstone	7.002	Parker_ini	161^3	0.12	5.4	19.0	2.4
			Parker_n1	82^3	0.11 (0.017)	4.0 (0.75)	10.7 (2.99)	2.6 (0.33)
			Parker_n2	65^3	0.12 (0.022)	3.8 (0.92)	10.4 (2.98)	3.0 (0.74)
			Parker_n3	55^3	0.12 (0.026)	3.7 (0.95)	9.0 (2.09)	3.0 (0.72)
			Parker_n4	41^3	0.11 (0.025)	3.2 (0.75)	6.8 (1.71)	3.4 (1.12)
			Parker_n5	37^3	0.12 (0.035)	3.3 (0.95)	6.8 (2.14)	3.6 (1.48)
Leopard	Sandstone	2.250	Leopard_ini	151^3	0.20	6.6	14.0	7.3
			Leopard_n1	77^3	0.18 (0.025)	4.3 (1.10)	5.5 (1.37)	2.1 (0.94)
			Leopard_n2	61^3	0.17 (0.061)	3.0 (1.32)	3.6 (1.35)	3.0 (1.38)
			Leopard_n3	51^3	0.18 (0.078)	2.4 (1.08)	3.2 (1.11)	3.1 (1.76)
			Leopard_n4	39^3	0.17 (0.123)	2.2 (0.95)	2.5 (1.43)	5.1 (3.91)
			Leopard_n5	35^3	0.18 (0.133)	2.0 (0.90)	2.3 (1.31)	5.3 (4.24)
Ketton	Carbonate	10.313	Ketton_ini	160^3	0.14	6.4	13.0	6.4
			Ketton_n1	81^3	0.14 (0.025)	4.1 (0.51)	6.1 (1.21)	8.8 (4.24)
			Ketton_n2	65^3	0.14 (0.024)	4.7 (0.43)	7.3 (0.79)	6.9 (3.15)
			Ketton_n3	54^3	0.13 (0.030)	4.1 (0.71)	5.7 (1.20)	9.0 (4.42)
			Ketton_n4	41^3	0.13 (0.034)	3.4 (0.78)	4.3 (1.31)	11.6 (5.61)
			Ketton_n5	37^3	0.13 (0.036)	3.3 (0.67)	3.9 (1.04)	14.1 (6.37)
C1_carb	Carbonate	7.125	C1_carb_ini	160^3	0.23	6.1	14.0	2.3
			C1_carb_n1	81^3	0.27 (0.090)	5.3 (1.41)	11.9 (3.61)	2.8 (0.48)
			C1_carb_n2	65^3	0.23 (0.088)	4.3 (1.12)	9.1 (2.58)	3.1 (0.83)
			C1_carb_n3	54^3	0.21 (0.087)	3.7 (0.98)	7.4 (2.46)	3.9 (1.39)
			C1_carb_n4	41^3	0.20 (0.080)	3.0 (0.85)	5.3 (1.43)	4.5 (1.37)
			C1_carb_n5	37^3	0.17 (0.079)	2.6 (0.58)	4.4 (0.98)	5.1 (2.61)
C2_carb	Carbonate	5.345	C2_carb_ini	121^3	0.15	3.6	10.0	2.1
			C2_carb_n1	62^3	0.12 (0.050)	2.5 (1.05)	5.9 (1.69)	2.4 (0.67)
			C2_carb_n2	49^3	0.12 (0.058)	2.6 (1.32)	4.6 (1.77)	4.1 (2.56)
			C2_carb_n3	41^3	0.14 (0.075)	3.0 (1.75)	4.5 (2.13)	4.0 (2.99)

22

553

Salt	Salt	1.881	Salt_ini	160^3	0.08	4.6	7.0	0.8
			Salt_n1	81^3	0.07 (0.017)	3.5 (0.72)	5.7 (1.07)	1.8 (1.02)
			Salt_n2	65^3	0.07 (0.025)	3.2 (1.27)	4.5 (1.42)	1.8 (0.90)
			Salt_n3	54^3	0.07 (0.032)	2.7 (0.81)	3.6 (1.20)	2.3 (1.39)
			Salt_n4	41^3	0.08 (0.053)	2.2 (0.84)	2.6 (0.95)	4.2 (3.65)
			Salt_n5	37^3	0.08 (0.062)	2.0 (0.59)	2.5 (1.05)	3.8 (2.73)
QSGS_iso	Synthetic	7.000	QSGS_iso_ini	100^3	0.30	7.7	20.0	2.4
			QSGS_iso_n1	51^3	0.28 (0.015)	6.6 (1.04)	13.5 (3.63)	3.3 (0.84)
			QSGS_iso_n2	41^3	0.28 (0.018)	6.1 (1.86)	10.0 (2.77)	3.6 (1.29)
			QSGS_iso_n3	34^3	0.29 (0.034)	5.2 (1.11)	7.4 (1.32)	4.2 (2.12)
			QSGS_iso_n4	26^3	0.29 (0.042)	3.6 (0.80)	4.7 (0.95)	5.4 (3.57)
			QSGS_iso_n5	23^3	0.29 (0.054)	3.5 (0.82)	4.3 (0.92)	4.8 (2.42)
QSGS_aniso	Synthetic	7.000	QSGS_aniso_ini	100^3	0.20	4.9	13.0	2.3
			QSGS_aniso_n1	51^3	0.17 (0.024)	4.3 (0.49)	7.2 (1.38)	3.3 (0.90)
			QSGS_aniso_n2	41^3	0.18 (0.040)	3.8 (0.58)	6.1 (1.30)	4.0 (1.89)
			QSGS_aniso_n3	34^3	0.19 (0.044)	3.3 (0.62)	4.8 (1.07)	4.3 (1.45)
			QSGS_aniso_n4	26^3	0.19 (0.055)	3.0 (0.89)	4.2 (1.11)	5.1 (2.38)
			QSGS_aniso_n5	23^3	0.19 (0.056)	2.7 (0.68)	3.5 (0.86)	5.9 (3.24)
Finney	Synthetic	7.844	Finney_ini	160^3	0.36	9.5	20.0	3.3
			Finney_n1	81^3	0.37 (0.008)	7.7 (0.37)	12.3 (1.47)	5.2 (2.09)
			Finney_n2	65^3	0.36 (0.023)	7.0 (0.43)	10.8 (1.53)	6.9 (3.42)
			Finney_n3	54^3	0.37 (0.029)	6.2 (0.47)	8.2 (1.17)	6.7 (3.77)
			Finney_n4	41^3	0.37 (0.037)	5.1 (0.62)	6.4 (1.09)	8.3 (3.98)
			Finney_n5	37^3	0.38 (0.045)	4.6 (0.71)	5.3 (1.05)	7.3 (3.89)
RG_theta60	Synthetic	6.000	RG_ini	160^3	0.17	6.2	12.0	2.2
			RG_n1	81^3	0.18 (0.012)	5.6 (0.27)	10.2 (1.54)	4.6 (2.39)
			RG_n2	65^3	0.19 (0.041)	5.3 (0.62)	8.4 (1.01)	4.2 (1.58)
			RG_n3	54^3	0.18 (0.059)	4.7 (0.75)	7.4 (1.75)	5.1 (2.16)
			RG_n4	41^3	0.22 (0.088)	4.2 (0.64)	5.5 (0.93)	6.0 (3.08)
			RG_n5	37^3	0.20 (0.093)	3.7 (0.80)	4.6 (1.20)	7.5 (3.62)

554

555 **Table A2** Results of geometric tortuosity for all the considered samples and relative error of the
556 percolation model with respect to the A* algorithm. Hydraulic tortuosity was computed from
557 velocity field numerically simulated for only the largest length scale for the sake of compari-
558 son.

n.	Sub-sample	L_s (µm)	No. sub-samples	τ_h	τ_g A*	τ_g Eq. (2)	*ARE* (%)	τ_g Eq. (3)	*ARE* (%)	τ_g Eq. (4)	*ARE* (%)	τ_g Eq. (5)	*ARE* (%)
1	Berea_ini	914.0	-	1.55	1.41	2.94	108.4	2.67	88.7	1.90	34.3	1.50	5.9
2	Berea_n1	465.0	50		1.41	2.59	83.6	2.36	67.2	1.79	27.0	1.25	11.5
3	Berea_n2	368.8	50		1.46	2.55	74.4	2.32	58.3	1.71	17.0	1.20	18.3
4	Berea_n3	310.0	50		1.46	2.80	91.3	2.51	71. 6	1.80	22.8	1.21	17.0
5	Berea_n4	235.2	47		1.44	2.85	98.1	2.51	74.9	1.81	25.8	1.15	19.8
6	Berea_n5	208.5	50		1.42	2.75	93.3	2.43	70.8	1.76	23.8	1.14	19.9
7	Benth_ini	1514.0	-	1.60	1.35	2.72	101.1	2.48	82.9	1.83	35.0	1.61	19.2
8	Benth_n1	771.1	50		1.41	2.87	103.4	2.60	84.5	1.88	33.2	1.34	4.8
9	Benth_n2	611.2	50		1.42	2.88	103.7	2.61	84.6	1.89	33.6	1.27	10.1
10	Benth_n3	517.2	50		1.44	2.93	103.4	2.65	84.0	1.90	32.2	1.24	13.7
11	Benth_n4	385.5	50		1.45	2.87	97.8	2.59	78.2	1.79	23.3	1.23	15.2
12	Benth_n5	347.9	49		1.46	3.03	107.7	2.70	85.3	1.83	25.4	1.18	19.0
13	Parker_ini	1127.3	-	1.92	1.64	4.57	178.8	3.77	129.9	2.30	40.5	1.76	7.2
14	Parker_n1	574.1	50		1.75	4.94	183.1	3.93	125.5	2.41	38.1	1.63	6.3
15	Parker_n2	455.1	44		1.71	4.69	174.5	3.80	122.4	2.41	41.2	1.65	3.5
16	Parker_n3	385.1	42		1.69	4.60	171.7	3.74	120.6	2.33	37.4	1.58	6.5
17	Parker_n4	287.1	35		1.66	4.61	177.4	3.76	126.2	2.32	39.7	1.52	8.5
18	Parker_n5	259.1	37		1.59	4.29	169.5	3.56	123.7	2.30	44.3	1.49	6.4
19	Leopard_ini	339.8	-	1.47	1.50	2.92	94.9	2.65	76.5	1.90	26.4	1.40	6.8
20	Leopard_n1	173.3	19		1.30	3.02	133.0	2.73	110.4	1.91	47.1	1.10	15.4
21	Leopard_n2	137.3	23		1.33	2.83	112.9	2.55	91.9	1.86	39.6	1.08	18.5
22	Leopard_n3	114.8	25		1.33	2.58	93.9	2.35	76.3	1.78	33.7	1.11	16.4
23	Leopard_n4	87.8	19		1.33	2.43	83.3	2.20	65.5	1.61	21.4	1.03	22.6
24	Leopard_n5	78.8	14		1.32	2.23	68.9	2.02	53.1	1.55	17.7	1.06	19.6
35	Ketton_ini	1650.0	-	1.53	1.38	4.03	192.2	3.45	150.6	2.17	57.4	1.38	0.4
36	Ketton_n1	835.3	50		1.38	4.09	197.1	3.46	151.3	2.21	60.5	1.25	9.6
37	Ketton_n2	670.3	50		1.39	4.00	187.3	3.41	144.8	2.24	61.1	1.23	11.4
38	Ketton_n3	556.9	50		1.42	4.38	208.3	3.61	154.3	2.24	58.0	1.19	16.1
39	Ketton_n4	422.8	47		1.40	4.39	214.7	3.60	157.5	2.14	53.3	1.12	19.5
30	Ketton_n5	381.6	19		1.41	4.12	192.9	3.44	145.0	2.18	54.9	1.12	20.2
31	C1_carb_ini	1140.0	-	1.58	1.42	2.54	78.2	2.31	62.4	1.80	26.1	1.46	2.6
32	C1_carb_n1	577.1	50		1.51	2.54	68.2	2.27	50.5	1.65	9.4	1.46	3.1
33	C1_carb_n2	463.1	45		1.56	2.91	86.4	2.57	64.5	1.89	20.9	1.48	5.5
34	C1_carb_n3	384.8	41		1.65	3.09	87.0	2.69	63.0	2.03	22.9	1.47	10.9
35	C1_carb_n4	292.1	28		1.50	3.12	107.5	2.68	78.1	1.90	26.5	1.47	2.3
36	C1_carb_n5	263.6	22		1.54	3.19	107.7	2.74	78.7	2.02	31.6	1.48	3.9

37	C2_carb_ini	646.7	-	1.41	1.50	3.76	151.0	3.28	119.0	2.11	41.2	1.68	12.4
38	C2_carb_n1	331.4	11		1.52	3.59	136.1	3.15	107.6	2.18	43.5	1.36	10.2
39	C2_carb_n3	219.1	14		1.41	2.85	101.7	2.56	81.2	2.05	44.8	1.25	11.7
40	Salt_ini	301.0	-	1.63	1.59	6.85	330.9	4.71	195.9	2.69	68.9	1.25	21.5
41	Salt_n1	152.4	28		1.54	6.74	338.2	4.66	202.9	2.70	75.7	1.28	17.1
42	Salt_n2	122.3	31		1.56	6.62	324.7	4.60	195.2	2.68	72.0	1.18	24.5
43	Salt_n3	101.6	24		1.57	6.64	321.9	4.57	190.5	2.63	66.8	1.15	27.1
44	QSGS_iso_ini	700.0	-	1.57	1.38	2.09	51.5	1.89	37.4	1.62	17.7	1.51	9.7
45	QSGS_iso_n1	357.0	50		1.43	2.24	56.3	2.03	42.1	1.66	15.9	1.37	4.5
46	QSGS_iso_n2	287.0	50		1.45	2.22	53.3	2.02	39.3	1.67	15.1	1.27	12.3
47	QSGS_iso_n3	238.0	50		1.43	2.18	52.5	1.98	38.5	1.66	15.9	1.20	16.2
48	QSGS_iso_n4	182.0	50		1.47	2.20	49.8	2.00	36.1	1.64	11.3	1.18	20.0
49	QSGS_iso_n5	161.0	50		1.45	2.22	53.6	2.02	39.4	1.62	12.1	1.15	20.4
50	QSGS_aniso_ini	700.0	-	1.60	1.57	2.90	84.4	2.63	67.1	1.89	20.4	1.59	0.8
51	QSGS_aniso_n1	357.0	50		1.53	3.35	119.5	2.97	94.6	1.96	28.2	1.30	14.7
52	QSGS_aniso_n2	287.0	50		1.55	3.25	110.1	2.87	85.5	1.89	22.4	1.28	17.0
53	QSGS_aniso_n3	238.0	50		1.55	3.24	108.7	2.84	83.2	1.85	19.1	1.25	19.7
54	QSGS_aniso_n4	182.0	50		1.52	3.33	119.6	2.89	90.7	1.89	24.6	1.29	15.2
55	QSGS_aniso_n5	161.0	50		1.43	3.30	130.6	2.87	100.5	1.83	28.1	1.26	11.5
56	Finney_ini	1255.0	-	1.25	1.27	1.82	43.2	1.64	29.2	1.51	19.1	1.37	8.2
57	Finney_n1	635.3	50		1.28	1.79	39.5	1.62	25.8	1.49	16.2	1.23	4.1
58	Finney_n2	509.8	50		1.29	1.81	40.0	1.63	26.3	1.50	16.4	1.21	6.4
59	Finney_n3	423.6	50		1.29	1.78	37.8	1.61	24.4	1.48	14.4	1.14	12.3
60	Finney_n4	321.6	50		1.30	1.80	37.9	1.62	24.5	1.47	12.7	1.11	14.6
61	Finney_n5	290.2	50		1.31	1.78	35.8	1.60	22.6	1.47	12.3	1.07	18.2
62	RG_ini	960.0	-	1.32	1.29	3.30	155.4	2.95	128.3	2.02	56.0	1.35	4.3
63	RG_n1	486.0	50		1.32	3.13	136.4	2.81	112.6	1.94	47.0	1.32	0.0
64	RG_n2	390.0	50		1.33	3.10	133.1	2.76	107.7	1.93	45.5	1.26	5.4
65	RG_n3	324.0	50		1.34	3.42	154.2	2.95	119.5	1.99	47.8	1.25	6.7
66	RG_n4	246.0	50		1.32	3.30	149.4	2.74	107.1	1.88	42.2	1.15	12.9
67	RG_n5	222.0	47		1.34	3.63	171.4	2.94	119.5	1.89	40.9	1.12	16.5

559
560

561 **Table A3** Sensitivity of geometric tortuosity to voxel dimension. For each case, the original
562 image size and characterization are highlighted in bold.

	Voxel size (μm)	ϕ (-)	Z_{max} (-)	Z_{ave} (-)	l_{min} (μm)	τ_g (-)
Berea	16.04	0.228	11	6.33	5.71	1.29
	10.69	0.236	11	6.88	3.84	1.24
	5.35	**0.227**	**16**	**9.02**	**2.24**	**1.28**
	2.67	0.227	15	7.99	1.16	1.32
	1.78	0.227	17	8.64	1.19	1.34
	1.34	0.227	26	10.98	0.76	1.43
	1.07	0.227	33	11.69	0.35	1.53
Bentheimer	28.21	0.204	8	4.57	13.48	1.32
	18.81	0.204	10	5.64	6.47	1.31
	9.40	**0.194**	**13**	**6.95**	**3.93**	**1.32**
	4.70	0.194	13	6.50	1.60	1.37
	3.13	0.194	15	6.42	1.11	1.46
	2.35	0.194	14	6.51	0.79	1.41
	1.88	0.194	16	7.16	0.64	1.43
Salt	5.64	0.070	3	2.03	8.20	1.39
	3.76	0.071	6	2.93	3.76	1.51
	1.88	**0.068**	**7**	**3.79**	**1.65**	**1.38**
	0.94	0.068	8	4.32	0.97	1.37
	0.63	0.068	8	4.15	0.46	1.40
	0.47	0.068	9	4.37	0.24	1.44
	0.38	0.068	21	9.09	0.14	1.43
RG	18.00	0.197	9	5.64	7.79	1.24
	12.00	0.195	7	5.13	7.35	1.16
	6.00	**0.181**	**10**	**5.51**	**2.48**	**1.33**
	3.00	0.181	11	5.54	2.75	1.38
	2.00	0.181	10	5.52	0.97	1.33
	1.50	0.181	11	5.85	0.90	1.34
	1.20	0.181	12	7.00	0.56	1.28
Ketton	30.94	0.133	3	1.98	20.73	1.49
	20.63	0.138	6	3.39	17.64	1.37
	10.31	**0.131**	**5**	**3.49**	**8.73**	**1.23**
	5.16	0.131	6	3.96	7.14	1.25
	3.44	0.131	7	4.45	3.31	1.26
	2.58	0.131	8	4.70	0.93	1.31
	2.06	0.131	10	5.47	1.57	1.33

Statements and Declarations

Funding

The authors declare that no funds, grants, or other support were received during the preparation of this manuscript.

Competing Interests

The authors have no relevant financial or non-financial interests to disclose.

Author Contributions

All authors contributed to the study conception and design. Material preparation, data collection and analysis were performed by Filippo Panini, Behzad Ghanbarian and Eloisa Salina Borello. Figures and tables were prepared by Filippo Panini and Eloisa Salina Borello. The first draft of the manuscript was written by Filippo Panini and Behzad Ghanbarian and all authors contributed to the final version of the manuscript. All authors read and approved the final manuscript.

Data Availability

Images used and analyzed in this study are available at the Digital Rocks Portal repository, https://www.digitalrocksportal.org/projects/, and the Pore-Scale Modelling research group repository at the Imperial College London,https://www.imperial.ac.uk/earth-science/research/research-groups/pore-scale-modelling/micro-ct-images-and-networks/

Acknowledgments

The authors are grateful to Cristina Serazio for her valuable contribution to the CFD simulations of hydraulic tortuosity.

References

1. Akaike, H. (1974), A new look at statistical model identification, IEEE Trans. Autom. Control, AC-19, 716–723.
2. Amien, M. N., Pantouw, G. T., Juliust, H., & Latief, F. D. E. (2019, August). Geometric tortuosity analysis of porous medium using simple neurite tracer. In IOP Conference Series: Earth and Environmental Science (Vol. 311, No. 1, p. 012041). IOP Publishing.
3. Aminpour, M., Galindo-Torres, S. A., Scheuermann, A., & Li, L.: Pore-scale behavior of Darcy flow in static and dynamic porous media. Physical Review Applied, 9(6), 064025 (2018).

4. An, S., Yao, J., Yang, Y., Zhang, L., Zhao, J., Gao, Y. (2016). Influence of pore structure parameters on flow characteristics based on a digital rock and the pore network model. Journal of Natural Gas Science and Engineering, 31, 156-163. https://doi.org/10.1016/j.jngse.2016.03.009
5. Ávila, J., Pagalo, J., & Espinoza-Andaluz, M. (2022). Evaluation of geometric tortuosity for 3D digitally generated porous media considering the pore size distribution and the A-star algorithm. Scientific Reports, 12(1), 19463.
6. Balberg, I. (1987). Recent developments in continuum percolation. Philosophical Magazine B, 56(6), 991-1003.
7. Blunt, M. J. (2017). Multiphase Flow in Permeable Media: A Pore-Scale Perspective. Cambridge University Press.
8. Cecen, A., Wargo, E. A., Hanna, A. C., Turner, D. M., Kalidindi, S. R., & Kumbur, E. C. (2012). 3-D microstructure analysis of fuel cell materials: spatial distributions of tortuosity, void size and diffusivity. Journal of The Electrochemical Society, 159(3), B299.
Chin. Phys. Lett. 21 (8), 1569–1571.
9. Clennell, M. B. (1997). Tortuosity: a guide through the maze. Geological Society, London, Special Publications, 122(1), 299-344. https://doi.org/10.1144/GSL.SP.1997.122.01.18
10. Dijkstra, E. W. (1959). A note on two problems in connexion with graphs. Numerische Mathematik 1, 269–271. https://doi.org/10.1007/BF01386390
11. Ferrari, A., & Lunati, I. (2013). Direct numerical simulations of interface dynamics to link capillary pressure and total surface energy. Advances in Water Resources, 57, 19-31.
12. Finney, J Finney Packing of Spheres. Digital Rocks Portal (April 2016). http://www.digitalrocksportal.org/projects/47
13. Foroughi, S., Bijeljic, B., & Blunt, M. J. (2021). Pore-by-pore modelling, validation and prediction of waterflooding in oil-wet rocks using dynamic synchrotron data. Transport in Porous Media, 138(2), 285-308.
14. Fu, J., Thomas, H. R., & Li, C. (2021). Tortuosity of porous media: Image analysis and physical simulation. Earth-Science Reviews, 212, 103439.
15. Garfi, G., John, C. M., Berg, S., & Krevor, S. (2020). The sensitivity of estimates of multiphase fluid and solid properties of porous rocks to image processing. Transport in Porous Media, 131(3), 985-1005.
16. Germanou L., Ho M.T., Zhang Y., Wu L., Intrinsic and apparent gas permeability of heterogeneous and anisotropic ultra-tight porous media, Journal of Natural Gas Science and Engineering, Volume 60, 2018, Pages 271-283, ISSN 1875-5100, https://doi.org/10.1016/j.jngse.2018.10.003.
17. Ghanbarian, B., & Cheng, P. (2016). Application of continuum percolation theory for modeling single-and two-phase characteristics of anisotropic carbon paper gas diffusion layers. Journal of Power Sources, 307, 613-623.
18. Ghanbarian, B., & Pachepsky, Y. (2022). Machine learning in vadose zone hydrology: A flashback. Vadose Zone Journal, 21(4), e20212.
19. Ghanbarian, B., Hunt, A.G., Ewing, R.P., Sahimi, M. (2013a) Tortuosity in porous media: a critical review. Soil science society of America journal 77(5):1461–1477 https://doi.org/10.2136/sssaj2012.0435
20. Ghanbarian, B., Hunt, A. G., Sahimi, M., Ewing, R. P., Skinner, T. E. (2013b). Percolation theory generates a physically based description of tortuosity in saturated and unsaturated porous media. Soil Science Society of America Journal, 77(6), 1920-1929.
21. Ghanbarian, B., Esmaeilpour, M., Ziff, R. M., & Sahimi, M. (2021). Effect of Pore-Scale Heterogeneity on Scale-Dependent Permeability: Pore-Network Simulation and Finite-Size Scaling Analysis. Water Resources Research, 57(12), e2021WR030664.

22. Ghanbarian, B., Lin, Q., & Pires, L. F. (2023). Scale dependence of tortuosity in soils under contrasting cultivation conditions. Soil and Tillage Research, 233, 105788.
23. Ghanbarzadeh, S. Synthetic Rock Salt. Digital Rocks Portal (August 2015). http://www.digitalrocksportal.org/projects/7
24. Ghanbarzadeh, S., Prodanovic, M., and Hesse, M. Texturally Equilibrated Pore Networks. Digital Rocks Portal (July 2016). http://www.digitalrocksportal.org/projects/65
25. Greenshields, C. (2022). Notes on Computational Fluid Dynamics: General Principles. CFD Direct Ltd.: Reading, UK. https://doc.cfd.direct/notes/cfd-general-principles/ ISBN-10 1399920782
26. Greenshields, C. (2023). OpenFOAM v11 User Guide. The OpenFOAM Foundation, London, UK. https://doc.cfd.direct/openfoam/user-guide-v11
27. Guibert, R., Nazarova, M., Horgue, P. *et al.* Computational Permeability Determination from Pore-Scale Imaging: Sample Size, Mesh and Method Sensitivities. *Transp Porous Med* 107, 641–656 (2015). https://doi.org/10.1007/s11242-015-0458-0
28. Hart, P.E., Nilsson, N.J., Raphael, B. (1968) A formal basis for the heuristic determination of minimum cost paths. IEEE transactions on Systems Science and Cybernetics 4(2):100–107
29. Huang, S., Yao, Y., Zhang, S., Ji, J., & Ma, R. (2018). A fractal model for oil transport in tight porous media. Transport in Porous Media, 121, 725-739.
30. Hunt, A., Ewing, R., & Ghanbarian, B. (2014). Percolation Theory for Flow in Porous Media (Vol. 880). Springer.
31. Hurvich C. M., Tsai C.-L., Regression and time series model selection in small samples, Biometrika, Volume 76, Issue 2, June 1989, Pages 297–307, https://doi.org/10.1093/biomet/76.2.297
32. Imperial College Consortium on Pore-scale Imaging and Modelling (2014a). Berea Sandstone. figshare. Dataset. https://doi.org/10.6084/m9.figshare.1153794.v2
33. Imperial College Consortium on Pore-scale Imaging and Modelling (2014b). C1 Carbonate. figshare. Dataset. https://doi.org/10.6084/m9.figshare.1189257.v1
34. Imperial College Consortium on Pore-scale Imaging and Modelling (2014c). C2 carbonate. figshare. Dataset. https://doi.org/10.6084/m9.figshare.1189258.v1
35. Imperial College Consortium on Pore-scale Imaging and Modelling (2015a). Bentheimer sandstone. https://imperialcollegelondon.app.box.com/v/iccpsim-bentheimer2015
36. Imperial College Consortium on Pore-scale Imaging and Modelling (2015b). Ketton carbonate. https://imperialcollegelondon.app.box.com/v/iccpsim-ketton2015
37. Jarrar, Z.A., Al-Raoush, R.I., Hannun, J.A., Alshibli, K.A., 2021. New model for estimating geometric tortuosity of variably saturated porous media using 3D synchrotron microcomputed tomography imaging. Soil Sci. Soc. Am. J. 85 (6), 1867–1879.
38. Kapitulnik, A., Aharony, A., Deutscher, G., Stauffer, D., 1983. Self similarity and correlations in percolation. J. Phys. A Math. Gen. 16 (8), L269–L274
39. Koponen, A., Kataja, M., & Timonen, J. V. (1996). Tortuous flow in porous media. Physical Review E, 54(1), 406.
40. Liu, Z., Wang, W., Cheng, W., Yang, H., & Zhao, D. (2020). Study on the seepage characteristics of coal based on the Kozeny-Carman equation and nuclear magnetic resonance experiment. Fuel, 266, 117088.
41. Massimiani A, Panini F, Marasso SL, Cocuzza M, Quaglio M, Pirri CF, Verga F, Viberti D (2023a) 2D microfluidic devices for pore-scale phenomena investigation: A review.Water 15(6):1222 https://doi.org/10.3390/w15061222
42. Massimiani A, Panini F, Marasso SL, Vasile N, Quaglio M, Coti C, Barbieri D, Verga F, Pirri CF, Viberti D (2023b) Design, fabrication, and experimental validation of microfluidic

devices for the investigation of pore-scale phenomena in underground gas storage systems. Micromachines 14(2):308 https://doi.org/10.3390/mi14020308
43. Montes, J. M., Cuevas, F. G., & Cintas, J. (2007). Electrical and thermal tortuosity in powder compacts. Granular Matter, 9, 401-406.
44. Muskat, M. (1938). The flow of homogeneous fluids through porous media. Soil Science, 46(2), 169.
45. Neumann, R., Andreeta, M., & Lucas-Oliveira, E. (2020, October 8). 11 Sandstones: raw, filtered and segmented data. Retrieved July 13, 2023, from www.digitalrocksportal.org
46. Nilsson NJ (1980) Principles of artificial intelligence. Tioga Pub. Co., Palo Alto, CA
47. Nilsson NJ (2014) Principles of artificial intelligence. Morgan Kaufmann
48. Niu, Y., Jackson, S. J., Alqahtani, N., Mostaghimi, P., & Armstrong, R. T. (2022). Paired and unpaired deep learning methods for physically accurate super-resolution carbonate rock images. Transport in Porous Media, 144(3), 825-847.
49. Panini F, Salina Borello E, Peter C, Viberti D (2022) Application of a* algorithm for tortuosity and effective porosity estimation of 2D rock images. In: Indeitsev DA, Krivtsov AM (eds) Advanced Problem in Mechanics II, Springer International Publishing, pp 519–530 https://doi.org/10.1007/978-3-030-92144-6_39
50. Patankar S.V. (1980). Numerical Heat Transfer and Fluid Flow. Taylor & Francis, Washington DC.
51. Peter C., E. Salina Borello, O. Baietto, R. Bellopede, F. Panini, A. Massimiani, P. Marini and Dario Viberti (2023). Quantitative Characterization of Marble Natural Aging through Pore Structure Image Analysis. Journal of Materials in Civil Engineering. Vol.35, n°9, pp. 4023286, Ascelibrary, https://ascelibrary.org/doi/pdf/10.1061/JMCEE7.MTENG-15161
52. Raeini, A. Q., Bijeljic, B., Blunt, M. J. (2017). Generalized network modeling: Network extraction as a coarse-scale discretization of the void space of porous media. Physical Review E, 96(1), 013312. https://doi.org/10.1103/PhysRevE.96.013312
53. Raeini, A. Q., Yang, J., Bondino, I., Bultreys, T., Blunt, M. J., & Bijeljic, B. (2019). Validating the generalized pore network model using micro-CT images of two-phase flow. Transport in Porous Media, 130(2), 405-424.
54. Rahmanian, M., & Kantzas, A. (2018). Stochastic generation of virtual porous media using a pseudo-crystallization approach. Journal of Natural Gas Science and Engineering, 53, 204-217.
55. Sahimi, M. (2023). Applications of Percolation Theory. Second Edition. Springer. 679 pp.
56. Salina Borello, E., Peter, C., Panini, F., Viberti, D. (2022) Application of A* algorithm for microstructure and transport properties characterization from 3d rock images. Energy 239:122151 https://doi.org/10.1016/j.energy.2021.122151
57. Schaap, M. G., and Leij, F. J. (1998). Database-related accuracy and uncertainty of pedotransfer functions. Soil Science, 163, 765–779.
58. Sobieski, W. (2022). Waterfall Algorithm as a tool of investigation the geometrical features of granular porous media. Computational Particle Mechanics, 9(3), 551-567.
59. Soulaine, C., Gjetvaj, F., Garing, C., Roman, S., Russian, A., Gouze, P., & Tchelepi, H. A. (2016). The impact of sub-resolution porosity of X-ray microtomography images on the permeability. Transport in Porous media, 113(1), 227-243.
60. Sun, W., Andrade, J. E., & Rudnicki, J. W. (2011). Multiscale method for characterization of porous microstructures and their impact on macroscopic effective permeability. International Journal for Numerical Methods in Engineering, 88(12), 1260-1279. https://doi.org/10.1002/nme.3220
61. Tang, G. H., & Lu, Y. B. (2014). A resistance model for Newtonian and power-law non-Newtonian fluid transport in porous media. Transport in Porous Media, 104, 435-449.

62. Teng, J., Yan, H., Liang, S., Zhang, S., & Sheng, D. (2021). Generalising the Kozeny-Carman equation to frozen soils. Journal of Hydrology, 594, 125885.
63. Viberti D, Peter C, Salina Borello E, Panini F (2020) Pore structure characterization through path-finding and lattice Boltzmann simulation. Advances in Water Resources 141:103609 https://doi.org/10.1016/j.advwatres.2020.103609
64. Wang, M., Wang, J., Pan, N., & Chen, S. (2007). Mesoscopic predictions of the effective thermal conductivity for microscale random porous media. Physical Review E, 75(3), 036702.
65. Wen, Z., Wang, Q., Ren, J., Zhang, L., & Yuan, Y. (2021). Dynamic gas diffusion model of capillary pores in a coal particle based on pore fractal characteristics. Transport in Porous Media, 140, 581-601.
66. Wu, J., Yu, B., & Yun, M. (2008). A resistance model for flow through porous media. Transport in Porous Media, 71, 331-343.
67. Yi, Z., Lin, M., Jiang, W., Zhang, Z., Li, H., Gao, J. (2017). Pore network extraction from pore space images of various porous media systems. Water Resources Research, 53(4), 3424-3445.
68. Yu, B.-M., Li, J.-H., 2004. A geometry model for tortuosity of flow path in porous media. Chinese Physics Letters, Volume 21, Number 8. DOI 10.1088/0256-307X/21/8/044.
69. Zhang S., G.H. Tang, WenQing Wang, Zen Li, Bo Wang, 2020, Prediction and evolution of the hydraulic tortuosity for unsaturated flow in actual porous media, Microporous and Mesoporous Materials, Volume 298, 110097, ISSN 1387-1811, https://doi.org/10.1016/j.micromeso.2020.110097.